2025,10(55s) e-ISSN: 2468-4376

https://www.jisem-journal.com/

**Research Article** 

# Simultaneous Maneuvering of Tethered Microsatellite Orbit and Tether Libration using a Model Reference Adaptive Control Scheme

#### Revanth Roy Kompally<sup>1</sup>, Weon Keun Song<sup>2,\*</sup>, Supun Dissanayaka<sup>3</sup>, Dong-Wook Lee<sup>4</sup>

<sup>1</sup>Sub Inspector, Information Technology and Communications, Telangana Police, India, (revanth.roy1204@gmail.com).

<sup>2,\*</sup>Coressponding Auhor, Assistant Professor, Department of Robotics and AI Engineering, King Mongkut's Institute of Technology

Ladkrabang, 1 Chalongkrung Road, Ladkrabang, Bangkok, Thailand 10520, (bauman98@naver.com).

<sup>3</sup>Instructor, Department of Robotics and AI Engineering, King Mongkut's Institute of Technology Ladkrabang, 1 Chalongkrung Road.

<sup>3</sup>Instructor, Department of Robotics and AI Engineering, King Mongkut's Institute of Technology Ladkrabang, 1 Chalongkrung Road, Ladkrabang, Bangkok, Thailand 10520, (supuntc@gmail.com).

<sup>4</sup>Postdoctoral Researcher, Convergence Medicine Asan Medical Center, Medical Imaging & Intelligent Reality Lab, 26, Olympic-ro 43 gil, Songpa-gu, Seoul, Korea, (dwleee1971@gmail.com).

#### **ARTICLE INFO**

#### **ABSTRACT**

Received: 28 Dec 2024 Revised: 14 Feb 2025 Accepted: 24 Feb 2025 This paper investigates the maneuvers of a tethered satellite system orbit disturbed by libration of a single elastic tether immediately after deployment, where the tether experiences no electrodynamic force. An effective Lyapunov-method-based multi-input and multi-output model reference adaptive control scheme exhibits good qualitative TSS orbit tracking error convergence; the perturbed TSS orbit tracks a reference orbit precisely with 3D tether pendular angle suppression. Although the simulated tether dynamic motion is limited to its libration, the proposed mathematical model with Gauss variational equations can consider the tether's pendular and dynamic motions together or separately. The latter realizes TSS orbital deviation by a non-conservative tether tension force acting on the primary body during tether libration. A feasibility study of the proposed control scheme through the maneuvers of the microsatellite under a zonal non-spherical harmonic gravitational perturbation ( $J_2$  perturbation) is conducted. Good tracking error convergence in the study indicates a potential high-accuracy control of the unstable TSS model using the proposed numerical procedure and control algorithm.

**Keywords**: TSS,  $J_2$  perturbation, MIMO MRAC, TSS orbital maneuver, suppression of tether libration.

#### **INTRODUCTION**

A tethered satellite system (TSS) is made of two cubic bodies connected by an elastic cable-type tether. Since the Gemini XI mission (David Darling, 2003), many space engineers have shown interest in TSS application, and the large body of TSS research has rapidly expanded in the last three decades. Typically, TSS-related research has focused on the following five topics: (1) tether dynamical modeling; (2) deployment and retrieval of a tether system and its control; (3) tether pendular angle analysis and control; (4) tether oscillation analysis and control; and (5) TSS trajectory generation and maneuver.

The dumb-bell tether model (Cosmo & Lorenzini, 1997) was one of the most important tether systems in early TSS research. However, a rigid rod-type tether (Larsen, 2010) was also applied to model TSSs and, in a study on TSS librations, Ellis and Hall (2010) modeled a TSS as two point masses connected by a rigid body. Furthermore, Williams (2009) studied the dynamics of a space tether using a model divided into a finite number of masses connected by viscoelastic springs.

Several studies have focused on a tether system in deployment or retrieval. For example, a simple nonlinear model for the motion of a tethered system in a retrieval process was proposed by Chernous'ko (1995). Further, Modi and Misra (1979) derived a general deployment dynamics formulation for a tether that incorporated the 3D tether libration and oscillation. A review article by Chen et al. (2013) introduced the feedback braking of a small expendable deployer system-2 for tether deployment, which limits the tether's residual libration to 4°. In addition, discussion by

2025,10(55s) e-ISSN: 2468-4376

https://www.jisem-journal.com/ Research Article

Misra (2008) focused on the control schemes for tether system stabilization during deployment and retrieval. Zabolotnov and Naumov (2012) studied the factors strongly related to the angular motion stability of a capsule relative to the direction of a tether in deployment. Iñarrea et al. (2014) achieved the stabilization of the periodic attitude motions of electrodynamic tethers in elliptically inclined orbits using two feedback control methods based on the time-delayed autosynchronization. Finally, Williams et al. (2009) discussed payload deployment via a tether system and examined the controllers for the flexible tether in the case of large disturbances using linear feedback gains such as the tether length and length rate.

Study of satellite trajectory dynamics requires detailed knowledge of orbital mechanics and numerical methods for solving differential equations. A series of studies on the orbit dynamics of satellites and asteroids (Dong et al., 2016; Gonçalves et al., 2015; Scheeres, et al., 1998a; Scheeres, et al., 1998b; Scheeres, 1999) have been conducted over the past two decades. For example, Gonçalves et al. (2015) considered a variety of gravitational and non-gravitational orbital disturbances. The Gauss variational equations (GVEs) were employed in a numerical analysis of satellite dynamics by taking account of the non-conservative perturbation forces, such as atmospheric drag and solar radiation (Dong et al., 2016). In another work (Jo et al., 2011), classical Keplerian orbital elements (CKOEs) and equinoctial orbital elements (EOEs) were used for solution of the Lagrange planetary equations (LPEs). It was clear that the LPEs with the EOEs are advantageous for long-term calculation compared to the LPEs with CKOEs in the case of relatively small eccentricity.

High tether flexibility increases the tether's structural instability and alters the primary body's acceleration, thereby deorbiting the TSS from the desired position. For TSS trajectory dynamic analysis and maneuvering, it is necessary to integrate separate mathematical models for the satellite and tether system, respectively. Thus, both the tether instability and TSS orbital deviation should be simultaneously predicted and suppressed. Therefore, there exists an extremely large body of literature on TSS control strategies (Misra, 2008; Misra and Modi et al., 1986; Zhao et al., 2014; Zhong and Zhu, 2014). In 2014, Zhao et al. (2014) proposed the thrust control algorithm for a TSS with a dumb-bell-type tether under orbital maneuvering. In their simulation, the tether slackness was eliminated, and the tether pendular angles were damped out. Furthermore, a piecewise two-phased optimal control algorithm for fast nanosatellite deorbit by an electrodynamic tether was proposed by Zhong and Zhu (2014). In the first stage, an open-loop control scheme was formulated for the tether libration only by assuming orbital elements as constants. The second stage focused on the closed-loop optimal control strategy based on a finite receding horizon control method, so as to track the desired reference trajectory subject to orbital perturbations.

Research on adaptive control for the speed and altitude of high-performance aircraft began in the 1950's. Notably, Tirop and Jingrui (2017) considered control of TSS pendular motion described by a classical dumb-bell model in an elliptic orbit; however, their discussion excluded the TSS deorbit induced by the tether libration. An adaptive controller with a nonzero constant plant parameter in the matrix form  $(B_p \neq 0)$  has been designed for a target plant (Polycarpou, 1996; Slotine & Li, 1991; Wang and Huang, 2005); it utilizes Lyapunov method-based control schemes. Furthermore, a series of remarkable studies on the design of dynamic regressor extension and mixing (DREM)-based adaptive controllers, including the model reference adaptive control (MRAC) scheme (Gerasimov et al., 2018a; Gerasimov et al., 2018b; Ortega et al., 2019), have largely reduced the prior knowledge required for B<sub>p</sub>. That is, in these proposed control schemes, only a full-rank condition is imposed on B<sub>p</sub>. The Lyapunov method-based multi-input and multi-output (MIMO) MRAC (Hashemi et al., 2015; Pankaj et al., 2011; Rao & Hassan, 2004) has attracted considerable research attention because of its intuitive mathematical concept and simple algorithm compared to proportional-integral-derivative (PID) controllers. Pankaj et al. (2011) compared the MIT and Lyapunov rules to develop an adaptation mechanism for a nonlinear single-input single-output (SISO) MRAC. Their analysis revealed that the Lyapunov rule reduced the MRAC configuration complexity, with physical realization of the applied system being more feasible than in the case of the MIT rule; this was despite the fact that the mathematical modeling of the system was simpler for the latter. Rao and Hassan (2004) developed new MRAC adaptive laws using non-quadratic Lyapunov candidate functions, which could improve the system output error converging to zero. Additionally, Hashemi et al. (2015) presented a tracking error convergence proof for a proposed MIMO MRAC design for potentially nonminimum phase square systems. Finally, El-samahy and Shamseldin (2018)

2025,10(55s) e-ISSN: 2468-4376

https://www.jisem-journal.com/ Research Article

showed the effectiveness of an MRAC scheme with a PID compensator in the context of reference model tracking for brushless DC motor tracking control, regardless of the load disturbance and parameter variations.

This study presents the Lyapunov method-based classical MIMO MRAC scheme, which enables both linear and nonlinear control to suppress TSS orbit deviation with the desired tether libration. A piecewise shape function is proposed, which can support the actual mechanical properties of an elastic tether only while withstanding its axial stretching and being free from flexural and shear rigidities. The proposed mathematical model incorporating the shape function can consider the tether pendular motion and the actual tether oscillation both together or separately. Thus, the interaction between the axial stretching and tether vibration, the tether libration, and the disturbance accelerations acting on the primary body can be considered. However, the restriction of the tether vibration does not allow a change in the magnitude of the tether tension force, as the coupling effect is not derived from all types of tether motions.

To successfully realize the TSS controller design, the feasibility of the GVEs and the proposed control scheme for the TSS orbit maneuvering is tested under the influence of the  $J_2$  perturbation. The fourteenth-order explicit Runge-Kutta method (RK14) is applied to those simulations. Good qualitative tracking performance is observed for microsatellite orbital maneuvering. Thus, it is expected that the application of the numerical method (including Jacobian linearization) combined with the proposed control scheme to TSS orbital maneuvers will yield high accuracy. The proposed adaptive controller is designed to suppress the TSS orbit deviation and 3D pendular motion of a single tether with length and diameter of 1.0 km and 2.0 mm, respectively, immediately after deployment. Here, the tether experiences no electrodynamic force based on the assumption that it can be perturbed by the deployment that results in tether swing. To realize the physical configuration, the mathematical model is established using the simple but innovative idea that the non-conservative tether tension force has a direct influence on the TSS orbital deviation as the tether swings. This model transforms the tether force to be equivalent to the disturbance accelerations in the GVEs. As a specific case of the adaptive controller with  $B_p \neq 0$  that was previously designed for a target plant (Polycarpou, 1996; Slotine & Li, 1991; Wang and Huang, 2005), in this study,  $k_1 \cdot B_p$  is tuned by multiplying an identity matrix  $B_p$  by  $k_1 = 0.01$ .

#### **METHODOLOGY**

## **TSS Mathematical Model**

The TSS consists of two end bodies, a primary body A and a secondary body B, which are connected by an elastic tether at  $P_A$  and  $P_B$ , respectively (see Fig. 1). The mass centers of A and B are  $G_A$  and  $G_B$ , respectively. The following assumptions are made for the mathematical modeling: (1) The central body is spherical in shape and its mass is distributed uniformly; (2) A and B have cubic shapes with homogeneous mass distributions as point masses, so that the influence of the gravitational forces of A and B on the Earth as well as on each other is nullified; (3) The Earth's magnetic dipole is oriented 11.5° from the Earth's rotational axis; (4) A and B are treated as rigid bodies; hence, their elastic vibration is negligible; (5) Rotational motions of A and B are neglected; (6) The tether is modeled as an elastic cable that can resist axial stretching only, with oscillation and twisting being ignored; (7) Only the tether elongation causes the tether tension force in the Earth's gravitational field; the direction of this force changes over time at  $P_A$  through the tether libration and perturbs the TSS's orbit.

The TSS mathematical model is developed based on the above assumptions. The position of A is given by the state variables of the CKOEs, as

$$O_{\mathcal{C}} = \{a(T), e(T), n(T), \Omega(T), \omega(T), \nu(T)\}^{T}$$
(1)

where  $O_{\Theta}$  defines the CKOE in a Keplerian orbit, a(T) is the semi-major axis, e(T) is the eccentricity, n(T) is the inclination,  $\Omega(T)$  is the right ascension of the ascending node, and  $\omega(T)$  and  $\nu(T)$  are the arguments of periapsis and true anomaly, respectively. Note that T indicates time. Three coordinate frames are used to handle the total TSS dynamics. The inertial frame  $F_N$  is the Earth frame, which is represented using the axes  $\widehat{n}_i$  with O as its center. The connection of the magnetic North Pole to the South Pole of the Earth gives  $\widehat{n}_3$ , and  $\widehat{n}_1 - \widehat{n}_2$  represents the equatorial plane. The orbit frame  $F_O$  is also established, in which  $F_O$  can be identified with the axes  $F_O$  as its center. Here,

2025,10(55s) e-ISSN: 2468-4376

https://www.jisem-journal.com/

#### **Research Article**

 $\hat{o}_3$  is the extension of  $\vec{r}_A(T)$  from O to  $G_A$ , while  $\hat{o}_2$  is given by the spin axis of A and  $\hat{o}_1$  is normal to the  $\hat{o}_2 - \hat{o}_3$  plane. Note that  $\vec{r}_A(T)$  denotes the position of  $G_A$  relative to O in  $F_N$ .  $\vec{r}_B(T)$  denotes the position of  $G_B$  relative to O in  $F_N$ . The tether system frame  $F_E$  is expressed by the  $\hat{e}_i$  axes. Here,  $\hat{e}_3$  directs from  $P_A$  to  $P_B$ . Further,  $\hat{e}_1$  is aligned perpendicularly to  $\hat{e}_3$  and  $\hat{e}_2$  is normal to the  $\hat{e}_1 - \hat{e}_3$  plane.  $\vec{P}_A(T)$  denotes the tether position  $P_A$  on A relative to  $G_A$  in  $F_O$ .  $\vec{P}_B(T)$  denotes the tether position  $P_B$  on  $P_A$  relative to  $P_A$  in  $P_A$  relative to  $P_A$  re

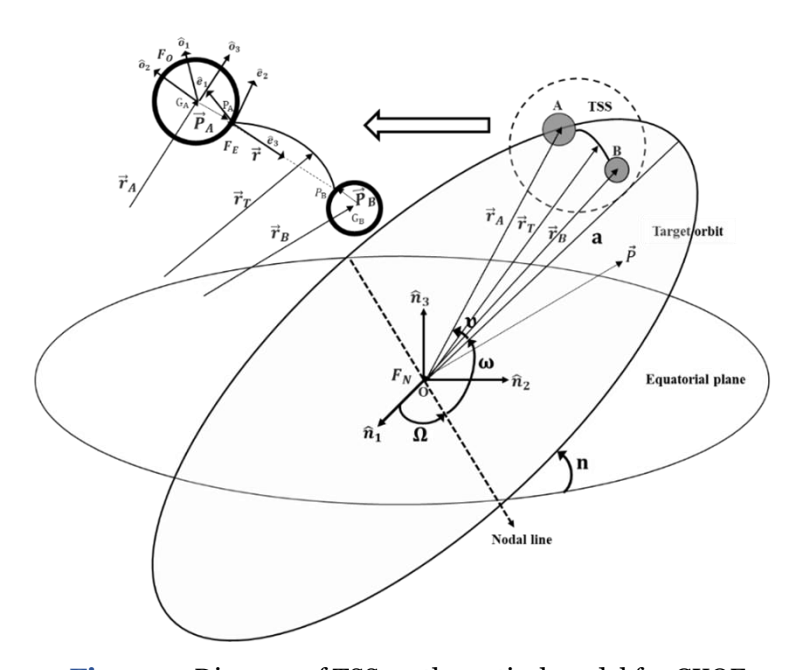


Figure 1. Diagram of TSS mathematical model for CKOE.

All the frames mentioned above can be related to each other using the direction cosine matrices shown in Eqs. 2a–2d. It is worth noting that the TSS dynamic analysis must be conducted in  $F_N$  through multiplication of the direction cosine matrices  $DCM_{N\leftarrow E}$  or  $DCM_{N\leftarrow O}$ , which map  $F_E$  and  $F_O$ , respectively, to  $F_N$ .

$$DCM_{N \leftarrow E} = DCM_{N \leftarrow O} \cdot DCM_{O \leftarrow E}$$
 (2a)

here,  $DCM_{0\leftarrow E}$  is the direction cosine matrix that maps  $F_E$  to  $F_O$ . A general rotation of a frame with axes "1", "2" and "3" can be characterized by Euler's angle rotation. Thus,  $DCM_{0\leftarrow N}$  and  $DCM_{E\leftarrow O}$  are defined, respectively, by 3-1-1 and 2-1 Euler's angle rotations.  $DCM_{N\leftarrow O}$  and  $DCM_{O\leftarrow E}$  are the inverse matrices, respectively, of  $DCM_{O\leftarrow N}$  and  $DCM_{E\leftarrow O}$ .

$$DCM_{O \leftarrow N} =$$

$$\begin{pmatrix} \cos(\theta(T))\cos(\Omega(T)) - \cos(n(T))\sin(\theta(T))\sin(\Omega(T)) & \cos(n(T))\cos(\Omega(T))\sin(\theta(T)) + \cos(\theta(T))\sin(\Omega(T)) & \sin(n(T))\sin(\theta(T)) \\ -\cos(\Omega(T))\sin(\theta(T)) - \cos(n(T))\cos(\theta(T))\sin(\Omega(T)) & \cos(n(T))\cos(\theta(T))\cos(\Omega(T)) - \sin(\theta(T))\sin(\Omega(T)) & \cos(\theta(T))\cos(n(T)) \\ & \sin(n(T))\sin(\Omega(T)) & -\cos(\Omega(T))\sin(n(T)) & \cos(n(T)) \end{pmatrix}$$

$$(2b)$$

 $DCM_{E\leftarrow O} = \begin{pmatrix} \cos{(\alpha(T))} & 0.0 & -\sin{(\alpha(T))} \\ -\sin{(\alpha(T))}\sin{(\beta(T))} & \cos{(\beta(T))} & -\cos{(\alpha(T))}\sin{(\beta(T))} \\ \cos{(\beta(T))}\sin{(\alpha(T))} & \sin{(\beta(T))} & \cos{(\alpha(T))}\cos{(\beta(T))} \end{pmatrix}$ (2c)

2025,10(55s) e-ISSN: 2468-4376

https://www.jisem-journal.com/

**Research Article** 

here,  $\alpha$  and  $\beta$  are the out-of-plane and in-plane pendular angles of the tether in  $F_{O_i}$  respectively. Further, n(T),  $\Omega(T)$ ,  $\omega(T)$ , and  $\nu(T)$  are the CKOEs constituting  $O_e$  (see section II.A.1).  $\theta(T) = \omega(T) + \nu(T)$  (2d).

#### **Equations of Motion of A**

This section presents the derivations of the six CKOEs (see Fig. 1 and Eqs. (3a)–(3i)). A complete set of equations of motion of A consists of the nonlinear differential equations governing the trajectory generation of  $G_A$  relative to  $F_N$ . The evolutions of the six CKOEs defined by the GVEs (Ellis, 2010; Jo et al., 2011) under the action of disturbance accelerations on A are given in the time domain as follows:

$$\dot{a}(T) = \frac{2a^2(T)}{h(T)} \left\{ \frac{p(T)}{r_A(T)} a_{DA1}(T) + e(T) \sin(\nu(T)) a_{DA3}(T) \right\}$$
(3a)

$$\dot{e}(T) = \frac{a_{DA1}(T)\{(p(T)+r_A(T))\cos(\nu(T))+e(T)r_A(T)\}+a_{DA3}(T)p(T)\sin(\nu(T))}{h(T)}$$
(3b)

$$\dot{n}(T) = \frac{a_{DA2}(T)\{r_A(T)\cos(\theta(T))\}}{h(T)}$$
(3c)

$$\dot{\Omega}(T) = \frac{a_{DA2}(T)\{r_A(T)\sin(\theta(T))\}}{\sin(n(T))h(T)}$$
(3d)

$$\dot{\omega}(T) = \frac{a_{DA2}(T) \left\{ r_A(T) \sin(\theta(T)) \cos(n(T)) \right\}}{h(T) \sin(n(T))} - \frac{a_{DA3}(T) p(T) \cos(\nu(T)) - a_{DA1}(T) \left\{ (p(T) + r_A(T)) \sin(\nu(T)) \right\}}{h(T) e(T)}$$
(3e)

$$\dot{v}(T) = \frac{a_{DA3}(T) \, p(T) \cos(v(T)) - a_{DA1}(T) \left\{ \sin(v(T)) \left( p(T) + r_A(T) \right) \right\}}{h(T) \, e(T)} + \frac{h(T)}{r_A^2(T)} \tag{3f}$$

where the orbital parameter of the osculating orbit is  $p(T) = a(T)(1 - e^2(T))$  (3g). The instantaneous orbit radius of a satellite is denoted by  $r_A(T) = \frac{p(T)}{1 + e(T)\cos(\nu(T))}$  (3h) and the specific angular momentum is  $h(T) = \sqrt{\mu p(T)}$  (3i). Further,  $\mu$  is the gravitational parameter of the central body (the Earth) and  $a_{DA1}(T)$ ,  $a_{DA2}(T)$ , and  $a_{DA3}(T)$  are the components of the disturbance acceleration  $\vec{a}_{DA}(T)$  acting on A. ( ) represents d/dT.

Note that  $a_{DA1}^{J2}(T)$ ,  $a_{DA2}^{J2}(T)$ , and  $a_{DA3}^{J2}(T)$  are the disturbance accelerations for the microsatellite due to the  $J_2$  perturbation. Thus,  $a_{DA1}(T)$ ,  $a_{DA2}(T)$ , and  $a_{DA3}(T)$  in Eqs. (3a)–(3f) should be replaced by

$$a_{DA1}^{J2}(T) = -\frac{3 \mu J_2 r_e^2(T)}{2r_A^4(T)} \{ \sin(n^2(T)) \sin(2 \theta(T)) \}$$
 (4a)

$$a_{DA2}^{J2}(T) = -\frac{3 \mu J_2 r_e^2(T)}{2 r_A^4(T)} \left\{ \sin(2n (T)) \sin(\theta(T)) \right\}$$
 (4b)

$$a_{DA3}^{J2}(T) = -\frac{3 \mu J_2 r_e^2(T)}{2 r_A^4(T)} \{ 1 - \sin(n^2(T)) \sin(\theta(T)^2) \}$$
 (4c)

where  $r_e(T)$  is the radius of the Earth. Substituting Eqs. (4a)–(4c) into Eqs. (3a)–(3f) allows solution of the CKOEs.

#### **Tether Tension**

In this study, the non-conservative tether tension force at  $P_A$  is considered, the direction of which can be changed over time via the tether libration. Finally, the TSS orbital deviation can be observed. Using the linear Kelvin-Voigt law of viscoelasticity, the total tension vector of the tether defined along its unit tangent direction in  $F_N$  through application of  $DCM_{N\leftarrow E}$  is

$$\vec{T}(S,T) = E \cdot A_O \left( \varepsilon_S + c \cdot \varepsilon_D(S,T) \right) \vec{\tau}(S,T) \tag{5}$$

where c is the structural damping constant, S is the arc length parameter along the unstretched tether, E is the Young's modulus of the tether,  $A_0$  is the cross-sectional area of the tether, and  $\vec{\tau}(S, T)$  is the unit tangent vector at a certain point on the tether. The dynamic strain of the tether is given by the Lagrange strain:

2025,10(55s)

e-ISSN: 2468-4376

https://www.jisem-journal.com/

**Research Article** 

$$\varepsilon_D(S,T) = \frac{\partial W(S,T)}{\partial S} + \frac{1}{2} \left\{ \left( \frac{\partial U(S,T)}{\partial S} \right)^2 + \left( \frac{\partial V(S,T)}{\partial S} \right)^2 + \left( \frac{\partial W(S,T)}{\partial S} \right)^2 \right\}$$
 (6)

here, U(S,T), V(S,T), and W(S,T) represent the normal, bi-normal, and longitudinal tether displacements, respectively, in  $F_N$ . In this study, the static strain of the tether  $\varepsilon_S$  can be considered zero when the following term (see Eq. (22c)) is constant over time:

$$c_{3,j}(T) = \frac{\|\vec{r}(s,T)\| \, l}{E \, A_O} \,. \tag{7}$$

In that case,  $\|\vec{T}(S,T)\|$  is time-invariant in  $F_E$  and  $\vec{T}(S,T)$  can be treated as the non-conservative tether tension force caused by the tether libration in  $F_N$ . Here, l is the total length of the tether in an unstretched configuration. The gravity acting on the tether, g=8.94841 (m/s<sup>2</sup>), and the mass of B,  $m_B=1.0$  (Kg), are applied to compute Eq. (5).

#### **Disturbance Acceleration Acting on the TSS**

Rearrangement of the translational motion of  $G_A$ , which is obtained by applying Newton's law to create  $\vec{a}_{DA}(T)$  in  $F_N$ , yields the following disturbance acceleration:

$$-\frac{\vec{r}_{GA}(T)}{m_A} + \vec{r}_A(T) = \frac{\vec{r}_{(0,T)}}{m_A} = \vec{a}_{DA}(T)$$
 (8)

where  $\vec{T}(0,T)$  is the tether tension force acting at  $P_A$ ,  $m_A$  is the mass of A, and  $\ddot{O}$  represents  $\frac{d^2}{dT^2}$ . The Earth's gravitational force acting on A is determined by the Newton universal gravitation law

$$\vec{F}_{GA}(T) = -\frac{m_A \mu}{r_A^3} \vec{r}_A(T) \tag{9}$$

where  $\vec{r}_A(T)$  with magnitude  $r_A$  relative to  $F_N$  is defined by

$$\vec{r}_A(T) = r_A \cos(n(T)) \cos(\omega(T) + \Omega(T) + \nu(T)) \hat{n}_1 + r_A \cos(n(T)) \sin(\omega(T) + \Omega(T) + \nu(T)) \hat{n}_2 + r_A \sin(n) \hat{n}_3$$
(10)

Finally,  $\vec{a}_{DA}(T)$  in Eq. 10, which causes the TSS orbit perturbation, must be redefined as follows:

$$\vec{a}_{DA}(T) = a_{DA1}(T)\,\hat{n}_1 + a_{DA2}(T)\hat{n}_2 + a_{DA3}(T)\,\hat{n}_3 \tag{11}$$

#### **Equation of Motion of Tether Pendular Angles**

Similar to the above, the translational motion of  $G_B$  is defined in  $F_N$  by

$$\frac{\vec{F}_{GB}(T)}{m_B} - \frac{\vec{T}(l,T)}{m_B} = \vec{r}_B(T)$$
 (12)

here,  $\vec{T}(l,T)$  is the tether tension force acting at  $P_B$ . The Earth's gravitational force acting on **B** is

$$\vec{F}_{GB}(T) = \frac{m_B}{r_B^2} \vec{r}_B(T) \tag{13}$$

where  $\vec{r}_B(T)$  with magnitude  $r_B$  relative to  $F_N$  is defined using the position vectors as

$$\vec{r}_A(T) + \vec{p}_A(T) + \vec{r}(l,T) - \vec{p}_B(T) = \vec{r}_B(T)$$
 (14)

2025,10(55s)

e-ISSN: 2468-4376

https://www.jisem-journal.com/

#### **Research Article**

here,  $\vec{r}(l, T)$  relative to  $F_N$  is given at S = l as the multiplication of  $\vec{r}(S, T)$  by  $DCM_{N \leftarrow E}$ , and the reidentification of  $\vec{p}_A(T)$  and  $\vec{p}_B(T)$  relative to  $F_N$  requires their multiplication by  $DCM_{N \leftarrow O}$ . The second derivative of  $\vec{r}(l, T)$  with respect to T yields

$$\ddot{\vec{r}}(l,T) = \ddot{r}_{l1}(l,T)\,\hat{n}_1 + \ddot{r}_{l2}(l,T)\,\hat{n}_2 + \ddot{r}_{l3}(l,T)\,\hat{n}_3 \tag{15}$$

where  $r_{l1}(l,T)$ ,  $r_{l2}(l,T)$ , and  $r_{l3}(l,T)$  are the components of  $\vec{r}(l,T)$ . The second derivative of Eq. (14) with respect to T and its rearrangement about  $\ddot{\vec{r}}(l,T)$  considering  $\ddot{\vec{r}}_A(T)$  in Eq. 10 and  $\ddot{\vec{r}}_B(T)$  in Eq. (12) gives

$$\vec{a}_{l}(T) = a_{l1}(T)\,\hat{n}_{1} + a_{l2}(T)\,\hat{n}_{2} + a_{l3}(T)\,\hat{n}_{3} \tag{16a}$$

here,  $a_{l1}(T)$ ,  $a_{l2}(T)$ , and  $a_{l3}(T)$  are the components of  $\vec{a}_l(T)$  acting at  $P_B$ . The equations of motion of the tether pendular angles,  $\alpha$  and  $\beta$ , are expressed as

$$\ddot{\vec{r}}(l,T) = \vec{a}_l(T) \tag{16b}$$

therefore,  $\ddot{r}_{l1}(l,T) = a_{l1}(T)$  (16c),  $\ddot{r}_{l2}(l,T) = a_{l2}(T)$  (16d) and  $\ddot{r}_{l3}(l,T) = a_{l3}(T)$  (16e). The motions of  $\alpha$  and  $\beta$  are observed, respectively, along  $\hat{e}_1$  and in the  $\hat{e}_2 - \hat{e}_3$  plane.

#### **Equations of Dynamic Motion of Tether**

The equations of dynamic motion of the tether can be defined by Newton's second law, considering the gravitational force and the electrodynamic force acting at dS due to an interaction of the current, i and Earth's magnetic field:

$$-\frac{\mu}{r_T^3}\vec{r}_T(S,T) + \frac{1}{\rho(T)}\frac{\partial \vec{T}(S,T)}{\partial S} + \frac{i}{\rho(T)}\frac{\partial \vec{r}(S,T)}{\partial S} \times \frac{\mu_m}{\rho^3} \left\{ \hat{u} - \frac{3\left(\hat{u}\cdot\vec{P}(T)\right)\vec{P}(T)}{\rho^2} \right\} - \ddot{\vec{r}}_A(T) - \ddot{\vec{p}}_A(T) = \ddot{\vec{r}}(S,T)$$
(17)

here,  $\rho(T)$  is the linear mass density for the unstretched tether, which is regarded as constant along the tether in this study. Further,  $\vec{r}_T(S,T)$  with the magnitude  $r_T$  is expressed as

$$\vec{r}_T(S,T) = \vec{r}(S,T) + \vec{p}_A(T) + \vec{r}_A(T)$$
 (18)

The Earth's magnetic field has a dipole centered at 0 with dipole axis  $\hat{u}$  and strength  $\mu_m$ .  $\vec{P}(T)$  is defined as

$$\vec{P}(T) = P\cos(\omega(T))\cos(\Omega(T))\hat{n}_1 + P\cos(\omega(T))\sin(\Omega(T))\hat{n}_2 + P\sin(\omega(T))\hat{n}_3$$
(19a)

here, P denotes the magnitude of  $\vec{P}(T)$ . The Earth's magnetic field with  $\hat{u}$  tilted at angle  $\Gamma$  relative to  $\hat{n}_3$  is constant.  $\theta$  denotes the angle between the  $\hat{u} - \hat{n}_3$  and  $\hat{n}_1 - \hat{n}_3$  planes, as shown in Fig. 2, and can be viewed as the local sidereal time of the unit dipole axis. Using the angles  $\theta$  and  $\Gamma$ ,  $\hat{u}$  must be defined as follows:

$$\hat{\mathbf{u}} = \cos \theta \sin \gamma \, \hat{\mathbf{n}}_1 + \sin \theta \sin \gamma \, \hat{\mathbf{n}}_2 + \cos \Gamma \, \hat{\mathbf{n}}_3 \tag{19b}$$

where  $\theta = \theta_0 + \omega_c T$  (19c) with  $\omega_c$  being the constant angular speed of the Earth and  $\theta_0$  is the value of  $\theta$  at T = 0. Further,

$$\gamma = 90 - \Gamma \tag{19d}.$$

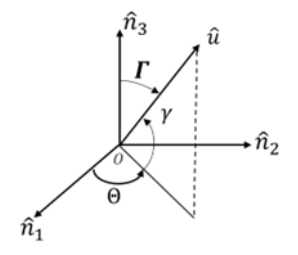


Figure 2. Unit dipole axis

2025,10(55s) e-ISSN: 2468-4376

https://www.jisem-journal.com/

**Research Article** 

#### Finite Element Method (FEM) Formulation

Using the FEM, to achieve discretization of a strong form (see Eq. 19), conversion to a weak form should be performed by multiplying the former by  $\emptyset_j$  (S) followed by integration over l. The substitution of  $\ddot{r}_A(T)$  and  $\ddot{r}_B(T)$  of Eqs. (8) and (12), respectively, along with the second derivative of  $\vec{r}(l,T)$  of Eq. (14) into the weak form gives the following through integration by parts for a tension-related term:

$$\int_{0}^{l} \vec{r}(S,T) \, \phi_{j}(S) \, dS + \frac{m_{B}}{\rho(T)} \vec{r}(l,T) \, \phi_{j}(l) = q_{1,j} \, \vec{r}_{A}(T) + q_{2,j} \, \vec{p}_{A}(T) + q_{3,i} \, \vec{p}_{B}(T) + \vec{h}_{j}(T) + \vec{k}_{j}(T)$$
(20a)

where,

$$q_{1,j} = -\int_0^l \phi_j(S) \, dS - \frac{m_B}{\rho(T)} \phi_j(l) - \frac{m_A}{\rho(T)} \phi_j(0)$$
 (20b)

$$q_{2,j} = -\int_0^l \phi_j(S) \, dS - \frac{m_B}{\rho(T)} \phi_j(l)$$
 (20c)

$$q_{3,j} = \frac{m_B}{\rho(T)} \emptyset_j(l) \tag{20d}$$

$$\vec{h}_{j}(T) = -\mu \left\{ \int_{0}^{l} \frac{\vec{r}_{T}(S,T)}{r_{T}^{3}} \phi_{j}(S) \, dS + \frac{m_{B}}{\rho(T)} \frac{\vec{r}_{B}(T)}{r_{B}^{3}} \phi_{j}(l) + \frac{m_{A}}{\rho(T)} \frac{\vec{r}_{A}(T)}{r_{A}^{3}} \phi_{j}(0) \right\}$$
(20e)

$$\vec{k}_{j}(T) = -\frac{1}{\rho(T)} \int_{0}^{l} \vec{T}(S, T) \frac{d\phi_{j}(S)}{dS} dS + \frac{i}{\rho(T)} \int_{0}^{l} \frac{\partial \vec{r}(S, T)}{\partial S} \times \vec{B}(T) \, \phi_{j}(S) \, dS$$
(20f)

Weddle's integration is applied for the discretization. Interpolation within the finite elements is achieved through a shape function for a single tether:

$$\emptyset_{j}(S) = \begin{cases} \frac{S - (j-2) \cdot lem}{lem}, \text{ for } (j-2) \cdot lem \le S \le (j-1) \ lem \\ \frac{j \cdot lem - S}{lem}, \text{ for } (j-1) \cdot lem < S \le j \cdot lem \end{cases}$$
(21)

where  $\emptyset_j$  (S) is a piecewise shape function, j represents the node number,  $lem = \frac{l}{ne}(m)$  is the length of each finite element, and ne is the total number of elements. The tether trail functions are given as

$$U(S,T) = \sum_{j=1}^{n_j} c_{1,j}(T) \cdot \phi_j(S)$$
 (22a)

$$V(S,T) = \sum_{i=1}^{n_j} c_{2,i}(T) \cdot \phi_i(S)$$
 (22b)

$$W(S,T) = \sum_{j=1}^{n_j} \mathbf{c}_{3,j}(T) \cdot \phi_j(S)$$
 (22c)

here,  $c_{1,j}(T)$ ,  $c_{2,j}(T)$ , and  $c_{3,j}(T)$  are time-dependent vectors and nj is the total number of nodes. Boundary conditions are imposed on the discretized system by fixing  $P_A$  and letting  $P_B$  be free. In this study, application of three finite elements to the tether during discretization creates a set of nine second-order nonlinear ordinary differential equations (ODEs).

#### **Jacobian Linearization**

After discretization, the total system of nonlinear first-order ODEs is expressed as

$$\dot{X}_p(T) = f_{ns}^N \left( X_p(T) \right) \tag{23a}$$

where  $X_p(T) = \{x_{p_1}(T), x_{p_2}(T), x_{p_3}(T), \dots, x_{p_{n_s}}(T)\}^T$  (23b) denotes a set of state variables in the total set of nonlinear ODEs describing an unstable plant.  $f_{n_s}^N$  represents a system of nonlinear ODEs, where  $n_s$  is the number of system variables. The Jacobian linearization of Eq. (23a), through Taylor series expansion with elimination of the negligible higher-order derivatives, is performed using the following equation

2025,10(55s)

e-ISSN: 2468-4376

https://www.jisem-journal.com/

**Research Article** 

$$f_{ns}^{L}(X_{p}(T)) = f_{ns}^{N}(X_{p}^{e}(T_{0})) + J \cdot (X_{p}(T) - X_{p}^{e}(T_{0}))$$
(24a)

here, the Jacobian matrix is given as

$$J = \begin{bmatrix} \frac{\partial f_1^N}{\partial x_{p_1}(T)} & \cdots & \frac{\partial f_1^N}{\partial x_{p_{ns}}(T)} \\ \vdots & \ddots & \vdots \\ \frac{\partial f_{ns}^N}{\partial x_{p_1}(T)} & \cdots & \frac{\partial f_{ns}^N}{\partial x_{p_{ns}}(T)} \end{bmatrix}_{X_n(T) = X_n^{\varrho}(T_0)}$$
(24b)

and  $X_p^e(T_0) = \left\{x_{p_1}^e(T_0), x_{p_2}^e(T_0), x_{p_3}^e(T_0), \dots, x_{p_{ns}}^e(T_0)\right\}^T$  (24c) is an equilibrium point where a set of initial conditions is applied at T = 0. Order reduction to construct Eq. (23a) is achieved for Eqs. (16c) and (16d) and discrete Eq. (20a), and the final number of equations is doubled.

#### Lyapunov-Method-Based MIMO MRAC Algorithm

In this study, the set of nonlinear differential equations defined by Eqs. 25a, b is used for both microsatellite dynamics and microsatellite orbital maneuvering. However, linearization is applied to the TSS dynamics and TSS orbital maneuvering (see Eqs. 26a–c). The proposed TSS control scheme should have the ability to suppress the tether's pendular motion and the TSS orbital deviation. This section discusses the design of the Lyapunov-method-based MIMO MRAC, which enables control of both unstable linear and nonlinear plants. Let us consider a continuous time-variant unstable system expressed by

$$\dot{X}_p(T) = -A_p \cdot X_p(T) - C_p \cdot f_p(T) + B_p \cdot u(T)$$
(25a)

where A<sub>p</sub>, B<sub>p</sub>, and C<sub>p</sub> are constant plant parameters in matrix form.

$$A_{p} = -I_{ns \times ns} \tag{25b},$$

$$B_{p} = k_{1} \cdot I_{\text{ns} \times \text{ns}} \tag{25c}$$

and

$$C_{\rm p} = I_{\rm ns \times ns} \tag{25d}.$$

here  $I_{ns\times ns}$  denotes an identity matrix, u(T) is the control input, and  $f_p(T)$  can be defined as

$$f_p(T) = -\left[A_p \cdot X_p(T) + f_{ns}^Q \left(X_p(T)\right)\right]$$
 (25e)

The superscript Q is set to N or L for a nonlinear or a linearized plant, respectively. A reference model is chosen to characterize the desired closed-loop system as

$$\dot{X}_m(T) = -A_m \cdot X_m(T) - C_m \cdot f_m(T) + B_m \cdot r(T)$$
(26a)

where,

$$X_m(T) = \left\{ x_{m_1}(T), x_{m_2}(T), x_{m_3}(T), \dots, x_{m_{n_s}}(T) \right\}^T$$
(26b)

is the set of state variables for the reference model.

$$r(T) = 0_{\text{nsx1}} \tag{26c}$$

denotes a reference signal and  $O_{ns\times 1}$  is the zero matrix. Further,  $A_m$ ,  $B_m$ , and  $C_m$  are constant parameters of the reference model in matrix form. A solution of the reference model is assumed to be a vector with the desired initial conditions such that

$$A_{\rm m} = -C_{\rm m} = -k_2 \cdot I_{\rm ns \times ns} \tag{26d}$$

2025,10(55s)

e-ISSN: 2468-4376

https://www.jisem-journal.com/

**Research Article** 

and B<sub>m</sub> can be a random matrix.

$$f_m(T) = I_{\text{ns} \times \text{ns}} \cdot X_m(T) \tag{26e}$$

can be a linear or nonlinear term in the reference model. Further,  $k_2$  is required to determine the  $P_L$  matrix for the adaptation laws (see Eqs. (29a)-(29d)) using the Lyapunov equation (see Eq. (29d)). Substituting Eqs. (26d) and (26e) into Eq. (26a) gives

$$\dot{X}_m(T) = 0 \tag{26f}$$

The change between the outputs of the unstable plant and reference model at every iteration is calculated as the tracking error  $\Delta(T)$ , given by

$$\Delta(T) = X_p(T) - X_m(T) \tag{27}$$

The control law is

$$u(T) = \hat{a}_X(T) \cdot X_p(T) + \hat{a}_r(T) \cdot r(T) + \hat{a}_f(T) \cdot f_p(T)$$
(28)

where  $\hat{a}_x(T)$ ,  $\hat{a}_r(T)$ , and  $\hat{a}_f(T)$  are the variable feedback gains. These can be identified using the following adaptation laws:

$$\hat{\boldsymbol{a}}_{\boldsymbol{X}}(T) = -\mathbf{B}_{\mathbf{p}}^{\mathsf{T}} \cdot \mathbf{P}_{\mathsf{L}} \cdot \Delta(\mathbf{T}) \cdot \mathbf{X}_{\mathbf{p}}(\mathbf{T})^{\mathsf{T}}$$
(29a)

$$\hat{\boldsymbol{a}}_{r}(\boldsymbol{T}) = -\mathbf{B}_{p}^{T} \cdot \mathbf{P}_{L} \cdot \Delta(\mathbf{T}) \cdot \mathbf{r}(\mathbf{T})^{T}$$
(29b)

$$\dot{\hat{a}}_f(T) = -B_p^T \cdot P_L \cdot \Delta(T) \cdot f_p(T)^T$$
(29c)

The adaptation laws necessary to enforce the closed loop stability of the control scheme are defined based on a quadratic Lyapunov function candidate. Here, PL is obtained from the Lyapunov equation:

$$A_m^T \cdot P_L + P_L \cdot A_m = -I_{ns \times ns}$$
 (29d)

To track the reference model, the iterative process should continue until the closed-loop dynamics yield zero  $\Delta(T)$ . The tracking error performance of the control scheme depends on fine tuning of  $k_1$  and  $k_2$  (see Eqs. 25c and 26d, respectively.)

#### **RESULTS**

## Validation of Lyapunov-method-based MIMO MRAC Scheme

A simulation on microsatellite orbital maneuvering as the feasibility study is reported to examine the potential of the TSS control in this section. It can be argued that the good qualitative result for the microsatellite orbit control indicates considerable promise for application of the proposed control scheme to the TSS orbital maneuvering. The microsatellite subjected to the  $J_2$  pertubation was considered based on the following initial values:  $a_0 = r_e + 300,000$  (m),  $e_0 = 0.07, n_0 = 50.0^{\circ}, \Omega_0 = 300.0^{\circ}, \omega_0 = 45.0^{\circ}, \text{ and } v_0 = 0.0^{\circ}.$  As input values for the simulation,  $r_e = 6.378.137$  (m),  $\mu = 3.986 \times 10^{14}$  (m<sup>3</sup>/s<sup>2</sup>), and  $J_2 = 1082.6267 \times 10^{-6}$  were considered. The control scheme included RK14 to trace solutions on not only microsatellite orbital maneuvering but the TSS position control.

Both the nonlinear and linearized models described by the GVEs were considered for the unstable plant. To achieve the orbital maneuver of the microsatellite, deorbit due to the  $J_2$  perturbation, the proposed control algorithm was applied. Note that, for the reference model, Eq. 28b must be exchanged with

$$X_m(T) = \{a_m(T), e_m(T), n_m(T), \Omega_m(T), \omega_m(T), \nu_m(T)\}^{\mathrm{T}}$$
(30)

and to identify the unstable plant, Eq. 25a should become the following, with ns = 6:

$$\{\dot{a}(T), \dot{e}(T), \dot{n}(T), \dot{\Omega}(T), \dot{\omega}(T), \dot{v}(T)\}^T = f_{ns}^Q \left( X_p(T) \right)$$
(31a)

2025,10(55s) e-ISSN: 2468-4376

https://www.jisem-journal.com/

**Research Article** 

here 
$$X_{\nu}(T) = \{a(T), e(T), n(T), \Omega(T), \omega(T), \nu(T)\}^{T}$$
 (31b)

and *Q* can be set to *L* or *N*. Eq. 26c should be replaced by the following expression for the linearized unstable plant:

$$X_p^e(T_0) = \{a_0(T_0), e_0(T_0), n_0(T_0), \Omega_0(T_0), \omega_0(T_0), \nu_0(T_0)\}^T$$
(31c)

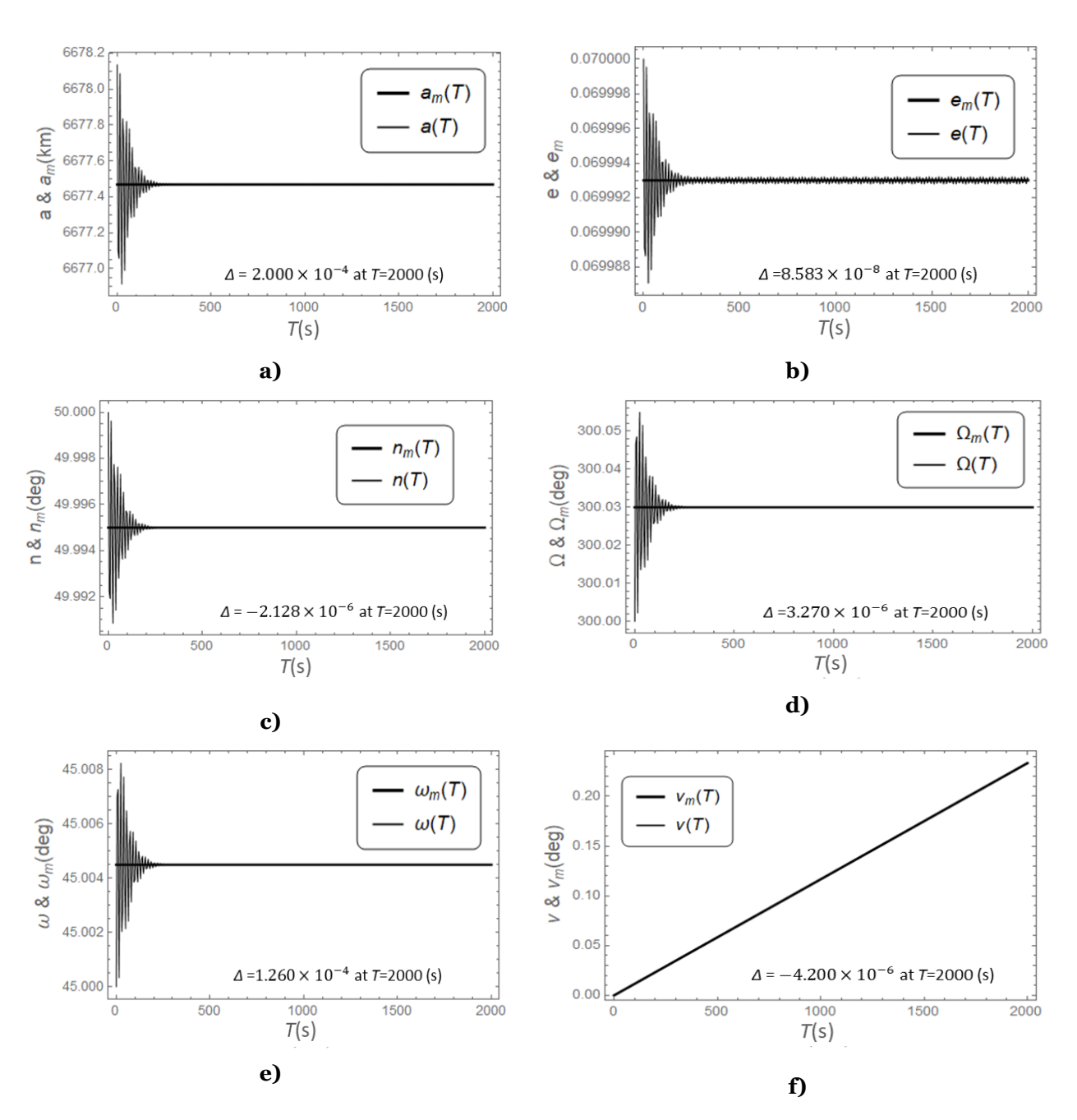


**Figure 3.** Tracking error convergence for linearized GVEs, for a)–f)  $a, e, n, \Omega, \omega$ , and v, respectively

2025,10(55s) e-ISSN: 2468-4376

https://www.jisem-journal.com/ Research Article

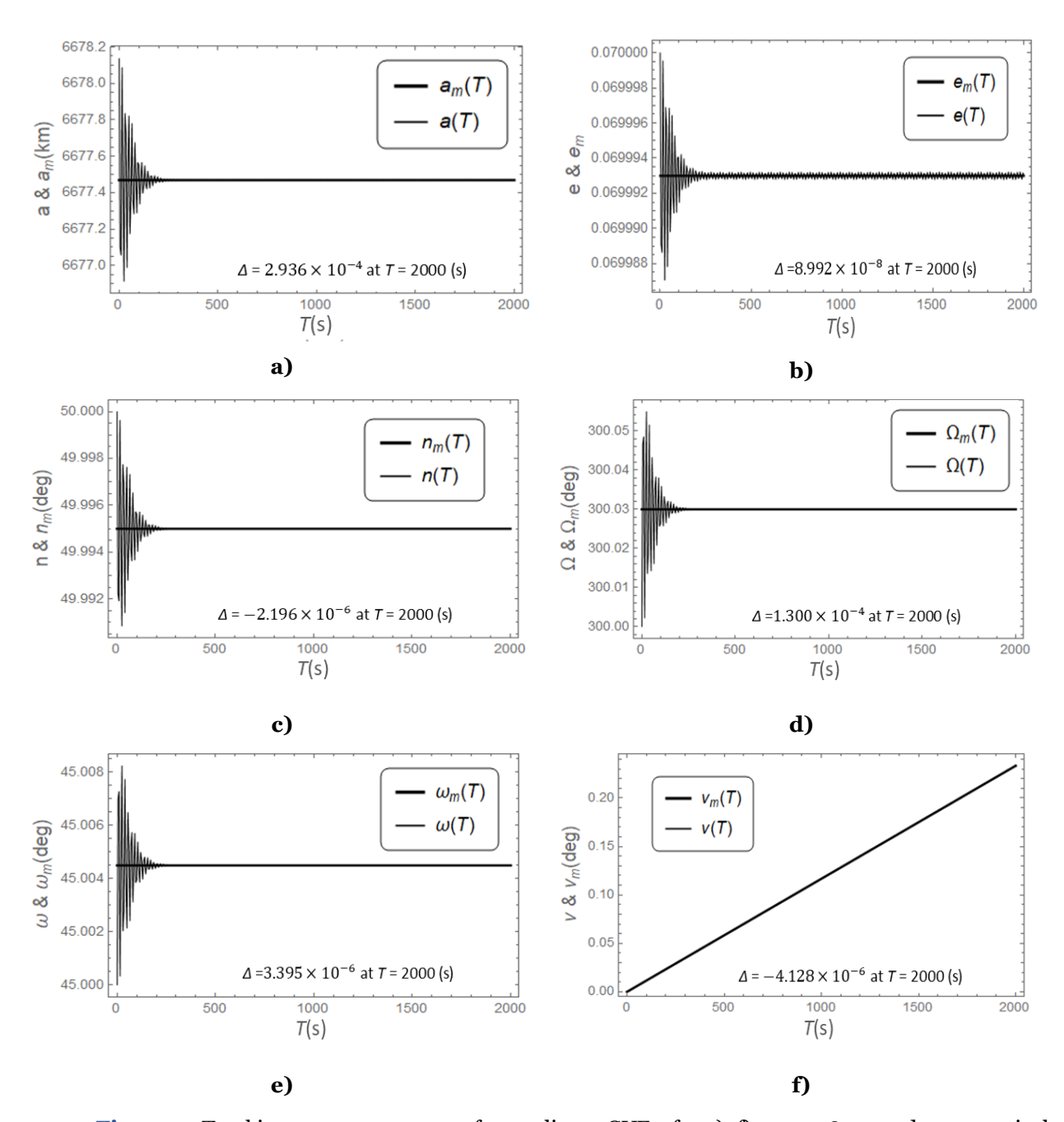


**Figure 4.** Tracking error convergence for nonlinear GVEs, for a)–f) a, e, n,  $\Omega$ ,  $\omega$ , and  $\nu$ , respectively

The tracking convergence performance of the proposed controller for the unstable model is shown in Figs. 3 and 4. These simulations were performed for 2,000 s using the step size of 0.0001 (s). Regarding the unstable plant, the initial and input values used for the microsatellite orbit dynamic analysis in section V were also applied to this analysis. For the reference orbit, the following values were used:  $a_m = a_0 - 0.0001 a_0$  (m),  $e_m = e_0 - 0.0001 e_0$ ,  $n_m = n_0 - 0.0001 n_0$  (deg),  $\Omega_m = \Omega_0 + 0.0001 \Omega_0$  (deg),  $\omega_m = \omega_0 + 0.0001 \omega_0$  (deg), and  $\nu_m = \frac{7}{60000} T$  (deg). In addition,  $k_1 = 0.01$ ,  $k_2 = 0.0001$ , and  $n_s = 6$  were used. Each response time was 250–260 (s), except for the  $\nu$  case, which appeared to converge in less than 1.0 (s). All the steady-state errors remained within the tolerance range of  $10^{-8}-10^{-4}$ . The identical tracking error performances of the linearized and nonlinear (see Figs. 3 and 4, respectively) plants for each CKOE clearly indicate the strong potential application of the linearized GVEs to TSS orbital maneuvers

2025,10(55s) e-ISSN: 2468-4376

https://www.jisem-journal.com/

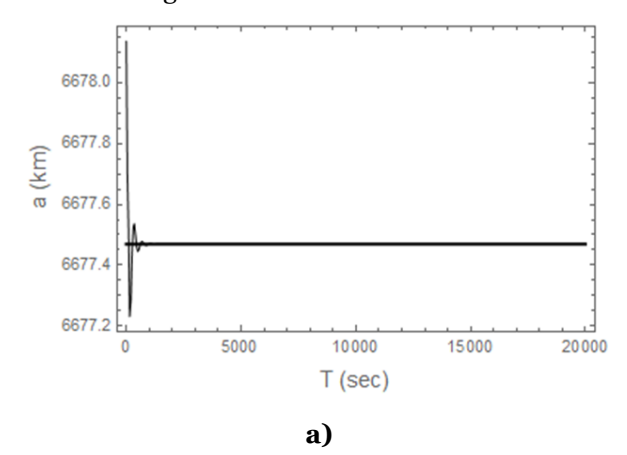
#### **Research Article**

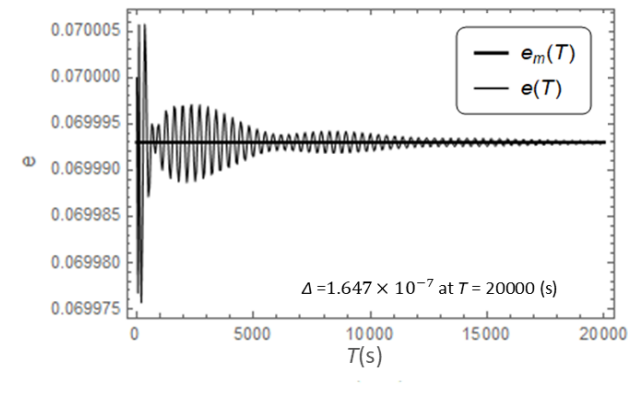
using the proposed control scheme. The results also validate the good tracking error performance of the proposed control scheme.

#### TSS ORBITAL MANEUVERS

This section reports on the TSS maneuvers using the linearized model. The influence of tether libration on the TSS orbital deviation is analyzed, and the tracking error performance of the control scheme for the TSS maneuvers is discussed. The TSS subjected to a non-conservative tether tension force of 8.94841 (N) was used. The mathematical model enabled the TSS to separately go through the in-plane and out-of-plane pendular motions of the tether or its libration in a 3D configuration. For the CKOEs, the initial values used for the microsatellite orbit control dynamic analysis were employed. The additional initial and input values were as follows:  $\theta_0 = 0.0^{\circ}$ ,  $\Gamma = 11.5^{\circ}$ ,  $P = r_e + 1,000,000 \text{ (m)}, \ \mu_m = 12.566 \times 10^{-7} \left(\frac{\text{H}}{\text{m}}\right), \ c = 0.5 \text{ (s)}, \ l = 1,000 \text{ (m)}, \ \rho = 2.5 \times 10^{-3} \ \left(\frac{\text{Kg}}{\text{m}}\right), E \cdot A = 55,000 \text{ (N)}, \ \rho = 2.5 \times 10^{-3} \ \left(\frac{\text{Kg}}{\text{m}}\right), E \cdot A = 55,000 \text{ (N)}, \ \rho = 2.5 \times 10^{-3} \ \left(\frac{\text{Kg}}{\text{m}}\right), E \cdot A = 55,000 \text{ (N)}, \ \rho = 2.5 \times 10^{-3} \ \left(\frac{\text{Kg}}{\text{m}}\right), E \cdot A = 55,000 \text{ (N)}, \ \rho = 2.5 \times 10^{-3} \ \left(\frac{\text{Kg}}{\text{m}}\right), E \cdot A = 55,000 \text{ (N)}, \ \rho = 2.5 \times 10^{-3} \ \left(\frac{\text{Kg}}{\text{m}}\right), E \cdot A = 55,000 \text{ (N)}, \ \rho = 2.5 \times 10^{-3} \ \left(\frac{\text{Kg}}{\text{m}}\right), E \cdot A = 55,000 \text{ (N)}, \ \rho = 2.5 \times 10^{-3} \ \left(\frac{\text{Kg}}{\text{m}}\right), E \cdot A = 55,000 \text{ (N)}, \ \rho = 2.5 \times 10^{-3} \ \left(\frac{\text{Kg}}{\text{m}}\right), E \cdot A = 55,000 \text{ (N)}, \ \rho = 2.5 \times 10^{-3} \ \left(\frac{\text{Kg}}{\text{m}}\right), E \cdot A = 55,000 \ \left(\frac{\text{Kg}}{\text{m}}\right),$  $c_{1,j}(T) = c_{2,j}(T) = 0.0 \text{ (m)}, c_{3,j}(T) = 0.162698 \text{ (m)}, \\ \dot{c}_{1,j}(0) = \dot{c}_{2,j}(0) = \dot{c}_{3,j}(0) = 0.0 \text{ (m/s)}, \\ \omega_c = 460.0 \text{ (m/s)}, \\ m_A = 0.0 \text{ (m/s)}$ 12.5 (Kg),  $m_B = 1.0$  (Kg).  $\vec{p}_A = (0.0, -2.5 \times 10^{-1}, 0.0)$  (m, m, m), and  $\vec{p}_B = (0.0, 5.0 \times 10^{-2}, 0.0)$  (m, m, m), defined in  $F_0$ . In addition, ne = 3 and ns = 8 were used for consideration of  $\alpha$  or  $\beta$ , while ns = 10 was used to investigate the effects of the combined angle of  $\alpha$  and  $\beta$ . The initial values used to investigate the effects of  $\alpha$  were the following:  $\alpha_0 = 0.1^{\circ}$ ,  $\beta_0 = 0.0^{\circ}$ ,  $\dot{\alpha}_0 = 0.3247$  (deg/s), and  $\dot{\beta}_0 = 0.0$  (deg/s). The initial values used to examine the effects of  $\beta$  were  $\alpha_0 = 0.0^\circ$ ,  $\beta_0 = 0.1^\circ$ ,  $\dot{\alpha}_0 = 0.0$  (deg/s), and  $\dot{\beta}_0 = 0.3247$  (deg/s). Finally, the initial values for consideration of the combined effect of  $\alpha$  and  $\beta$ were  $\alpha_0 = 0.1^{\circ}$  ,  $\beta_0 = 0.1^{\circ}$  ,  $\dot{\alpha}_0 = 0.3247 \, (\text{deg/s})$  ,  $\dot{\beta}_0 = 0.3247 \text{ (deg/s)}.$ 

Based on the result of the feasibility study, the linearized unstable TSS model was used for application of the proposed control scheme. For the case of an unstable plant, the initial and input values used for the TSS orbit dynamics were applied to the analysis. The initial values for the reference model were as follows:  $a_m = a_0 - 0.0001 \, a_0(\mathrm{m})$ ,  $e_m = e_0 - 0.0001 \, e_0$ ,  $n_m = n_0 - 0.0001 \, n_0(\mathrm{deg})$ ,  $\Omega_m = \Omega_0 + 0.0001 \, \Omega_0(\mathrm{deg})$ ,  $\omega_m = \omega_0 + 0.0001 \, \omega_0(\mathrm{deg})$ , and  $\nu_m = 0.0001 \, T(\mathrm{deg})$ . To consider the  $\alpha$  effects,  $\alpha_m = \alpha_0 - 0.0001 \, \alpha_0(\mathrm{deg})$  and  $\dot{\alpha}_m = \dot{\alpha}_0 - 0.0001 \, \dot{\alpha}_0(\mathrm{deg}/\mathrm{s})$  were used. To investigate the  $\beta$  effects,  $\beta_m = \beta_0 - 0.0001 \, \beta_0(\mathrm{deg})$  and  $\dot{\beta}_m = \dot{\beta}_0 - 0.0001 \, \dot{\beta}_0(\mathrm{deg}/\mathrm{s})$  were used. Further,  $k_1 = 0.01$  and  $k_2 = 0.00023218$  were employed to tune the plant input gain. Finally, ns = 8 was used for investigation of the effects of  $\alpha$  or  $\beta$  only, while ns = 10 was employed when the effects of the  $\alpha$  and  $\beta$  combined angle were considered.





b)

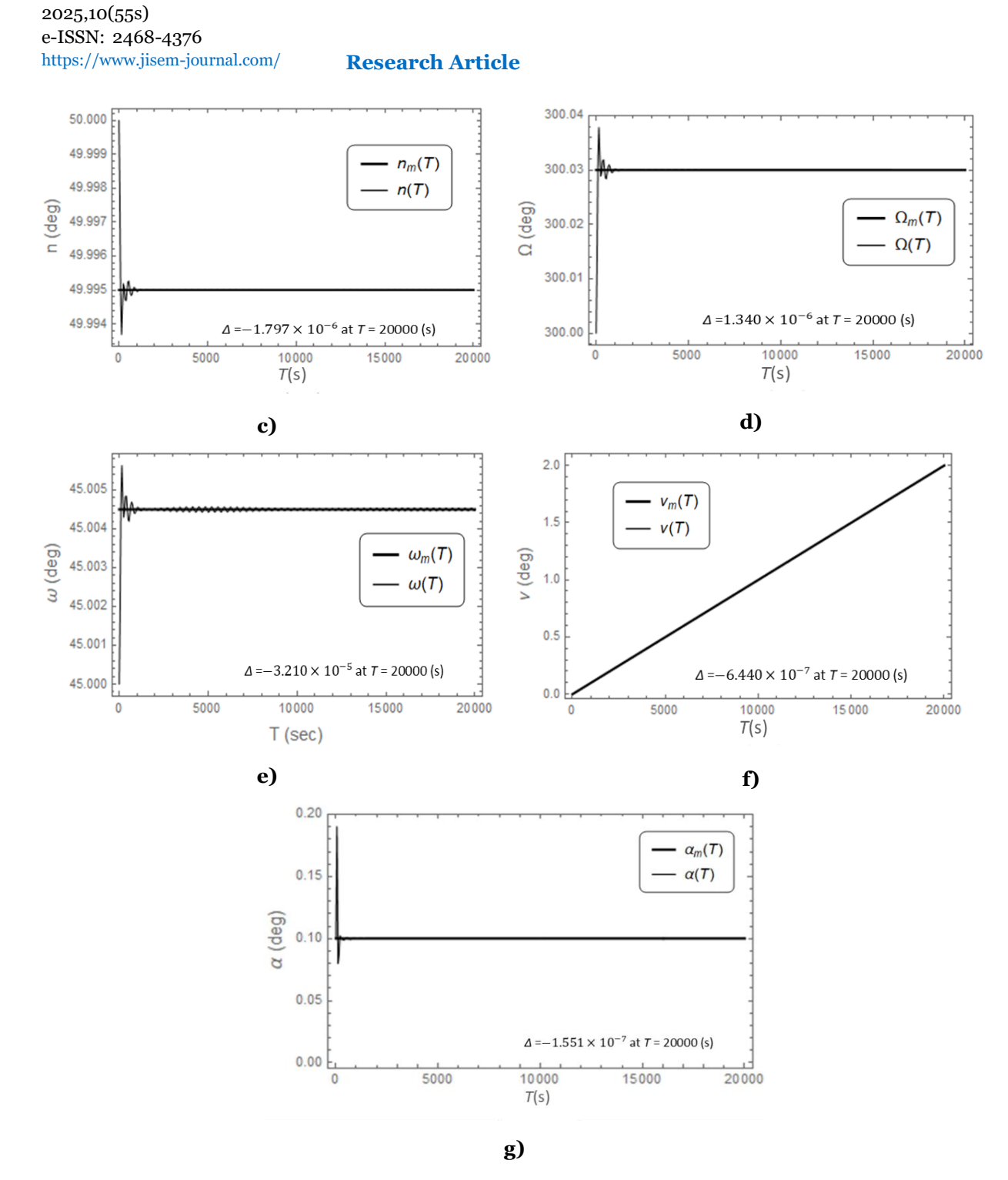


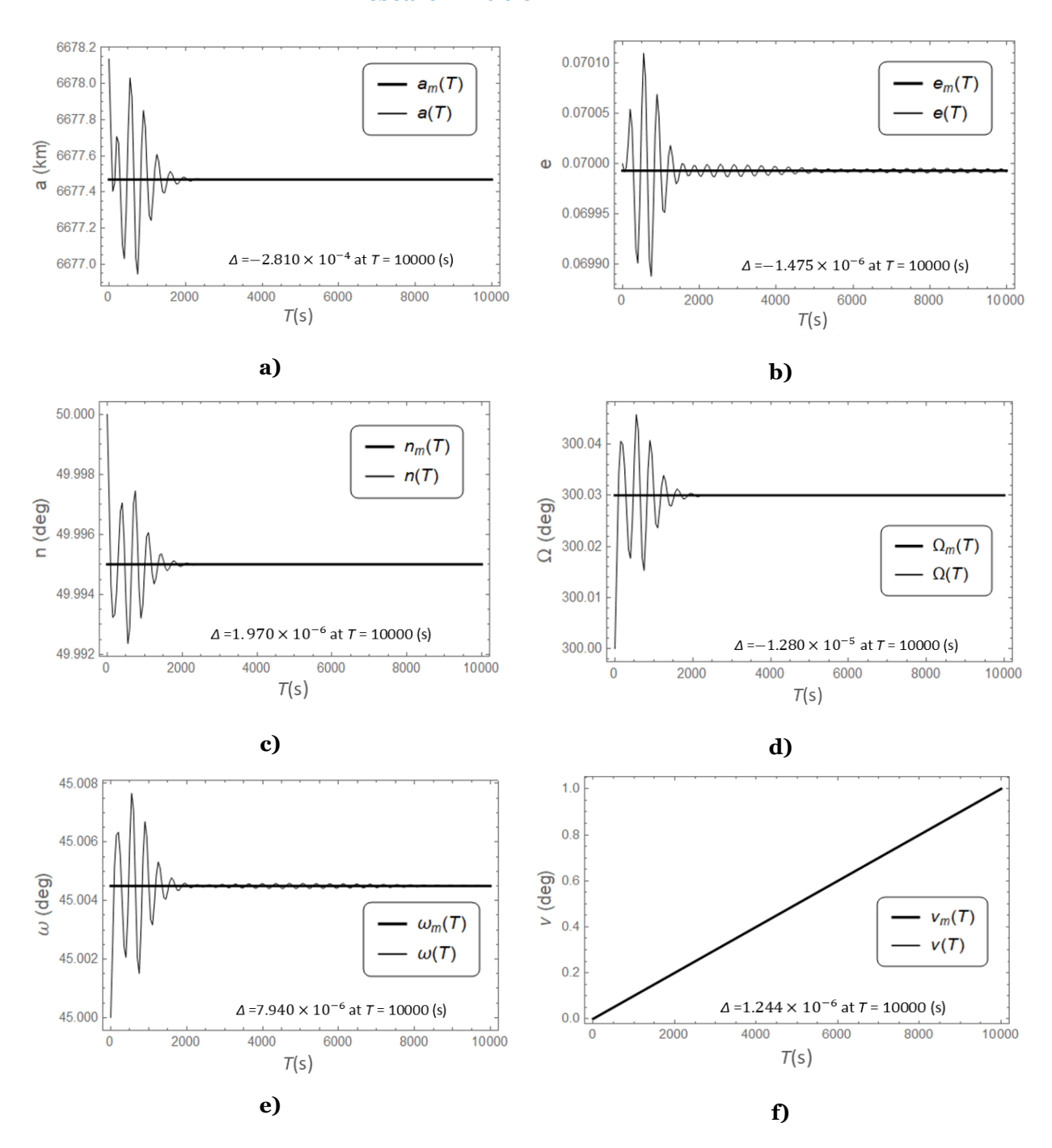
**Figure 5.** Tracking error convergence for simultaneous control of  $\alpha$  and TSS orbit perturbed by  $\alpha$ , for a)–g)  $\alpha$ , e, n,  $\Omega$ ,  $\omega$ ,  $\nu$ , and  $\alpha$ , respectively

2025,10(55s)

e-ISSN: 2468-4376

https://www.jisem-journal.com/

#### **Research Article**



2025,10(55s) e-ISSN: 2468-4376

https://www.jisem-journal.com/

#### **Research Article**

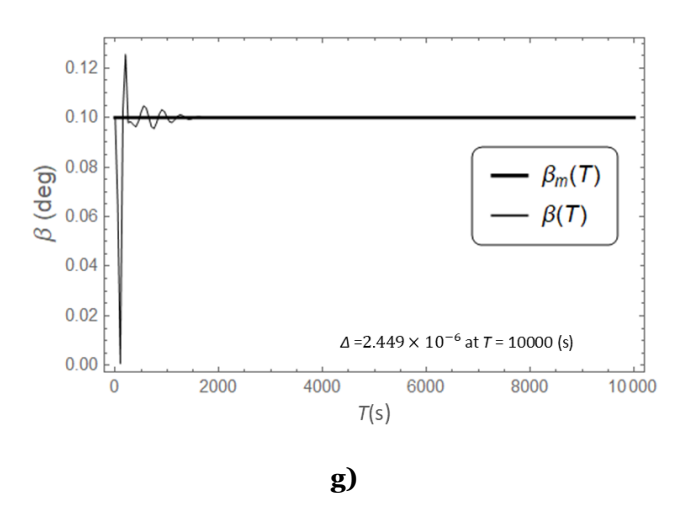
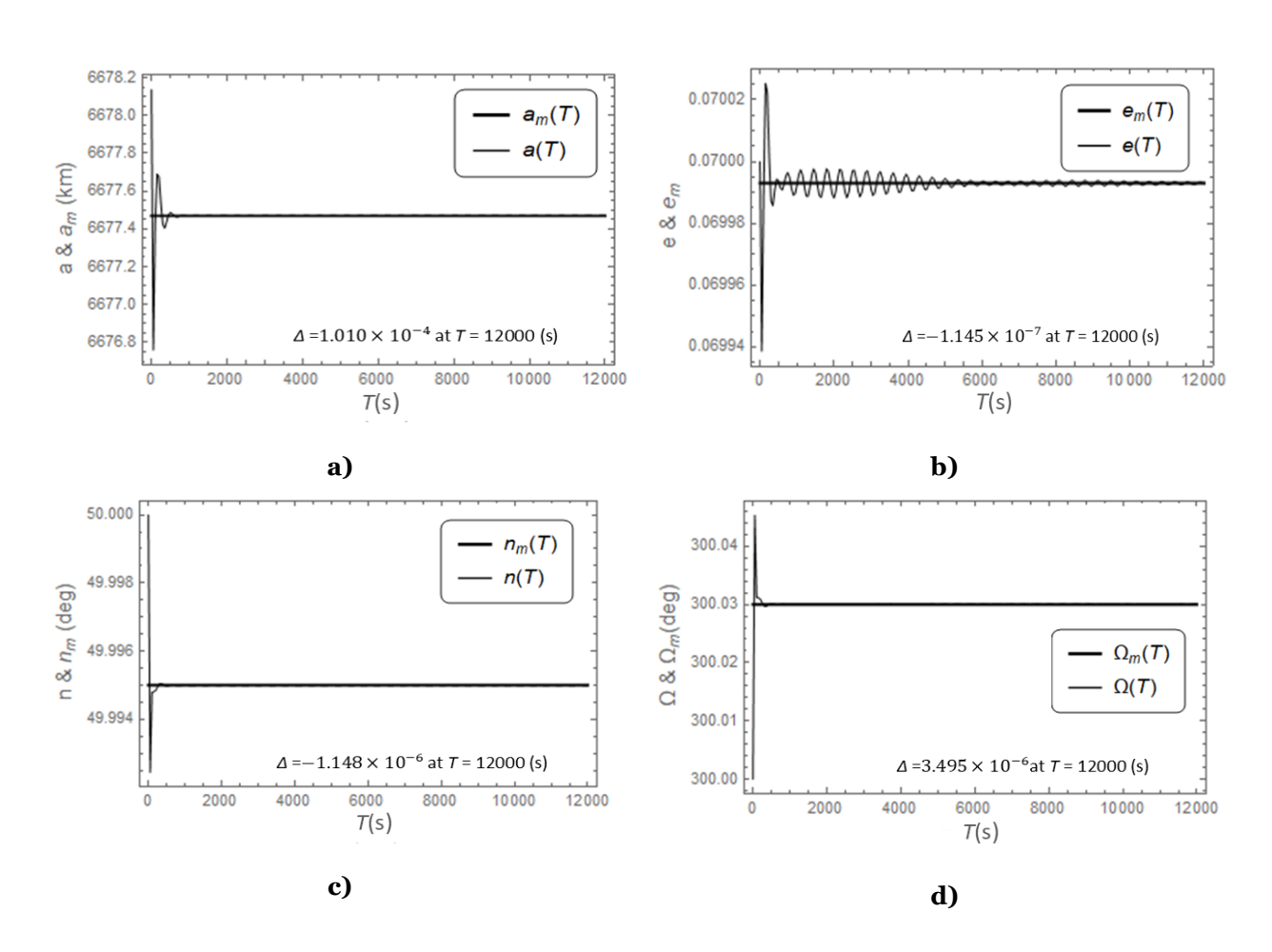


**Figure 6.** Tracking error convergence for simultaneous control of  $\beta$  and TSS orbit perturbed by  $\beta$ , for a)–g) a, e, n,  $\Omega$ ,  $\omega$ ,  $\nu$ , and  $\beta$ , respectively



2025,10(55s) e-ISSN: 2468-4376



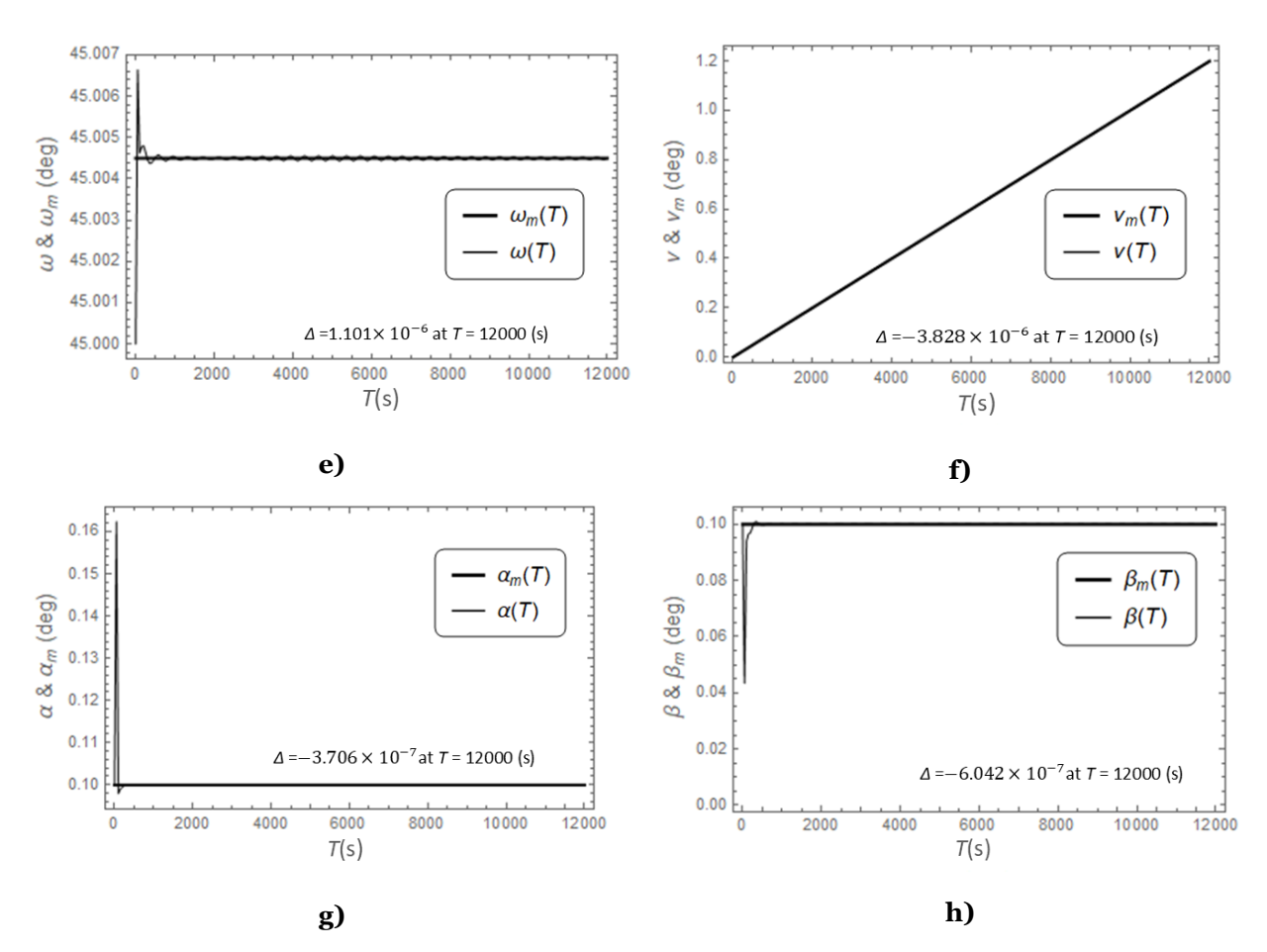


Fig. 5 shows the TSS orbital maneuvers obtained when the CKOEs and  $\alpha$  are controlled simultaneously by the control scheme. In Fig. 6, the results for simultaneous control of both the TSS orbital position and  $\beta$  are shown. Finally, Fig. 7 displays the orbital maneuvers of the TSS perturbed by the combined angle of  $\alpha$  and  $\beta$ . In Figs. 5–7, all the tracking errors converge within the limit of  $10^{-4}$ . Further, it is apparent from Fig. 5 that the controller stabilizes all plant outputs (except for e) in less than 1,000 (s). In detail,  $\alpha$  and e become stable after approximately 240 and 15,000 (s), respectively, with  $\alpha$  increasing by 0.19° and stabilizing within the range of  $10^{-7}$  degree. In Fig. 6, for the  $\beta$  case, it is observed that stabilization of a, n,  $\Omega$ , and  $\omega$  requires almost double the time periods of those reported in Fig. 5. However, e stabilizes more quickly under the influence of  $\beta$  than  $\alpha$ . It should be noted from Fig. 7 that all plant outputs (except for e and v) stabilize very quickly after exhibiting one or two peak overshoots. Hence, the control scheme is more effective for the maneuvers of the TSS allowing for the combined pendular angle of  $\alpha$  and  $\beta$  compared to the individual pendular angles. The tracking error performance is so sensitive to  $k_2$  for suppression of the TSS orbital deviation and the tether pendular angles that highly precise turning of  $k_2$  is required for the controller, even to eight decimal places.

## DISCUSSION

The orbital deviation of a TSS subjected to a non-conservative tether tension force was observed, and simultaneous suppression of both the tether pendular angles and the TSS orbital deviation was achieved using the proposed control scheme. The key findings of this work are listed below.

2025,10(55s) e-ISSN: 2468-4376

https://www.jisem-journal.com/ Research Article

- (1) Good tracking error performance was observed based on the microsatellite orbit maneuvering, which indicates the strong potential application of the proposed numerical approach and control scheme to TSS maneuvering.
- (2) The TSS orbit perturbation analysis clearly indicates that a and e deviate more strongly under the influence of  $\alpha$  compared to  $\beta$ , and that interaction of  $\alpha$  and  $\beta$  suppresses  $\alpha$  in a short period of time.
- (3) In this investigation, the coupling effect due to interaction of the pendular and dynamic motions of the tether was unquestionably limited because of the simplification of the tether's dynamic behavior. That is, the energy exchange through the couplings in the differential equations, which describe the actual interactions of the tether oscillation and libration over time, was not wholly considered, and only a one-way interaction between the tether tension force and tether libration was achieved.
- (4) Both the TSS orbital maneuvering and the suppression of the tether libration were well achieved using both the proposed control scheme and the numerical approach. Implementation of the control scheme with  $k_1$  = 0.01 and  $k_2$  = 0.00023218 yielded good tracking error convergence for the linearized unstable TSS model incorporating the plant outputs, such as  $\alpha$ ,  $\beta$  and the TSS orbital-position-related elements. Thus, the perturbed TSS tracks the desired orbit effectively while the controller simultaneously attenuates the tether pendular motion. Further, this analysis revealed that the unstable TSS orbit stabilizes more quickly to the desired orbit when the TSS allows the combined pendular angle of  $\alpha$  and  $\beta$  rather than each pendular angle.
- (5) The proposed control scheme requires very sensitive and precise turning of  $k_2$  for desired suppression of both the TSS orbital deviation and tether pendular angles.

In the simulations, the tether dynamic motion was limited to the tether libration (as noted in point (3) above). As a result, the coupled effect of all the tether motions were not reflected in changing the magnitude of the tether tension force at every single time step, which caused an actual disturbance and deorbited the TSS. The combined effect of the tether oscillation and the tether pendular motion on the TSS orbital deviation will be treated by the present authors in a series of separate research articles, using the mathematical model presented herein. In addition, the future research will investigate a link between the distributed form of the electrodynamic force along the tether and trajectory of the TSS while the proposed control scheme is applied to suppress the tether vibration.

#### **REFRENCES**

- [1] Chen, Y., Huang, R., Ren, X., He, L., & He, Y. (2013). History of the Tether Concept and Tether Missions: A Review. *International Scholarly Research Notices*, 2013(1), 502973. https://doi.org/10.1155/2013/502973
- [2] Chernous'ko, F. L. (1995). Dynamics of retrieval of a space tethered system. *Journal of Applied Mathematics and Mechanics*, *59*(2), 165–173. https://doi.org/10.1016/0021-8928(95)00020-P
- [3] Cosmo, M. L., & Lorenzini, E. C. (1997). *Tethers in Space Handbook* (NASA/CR-97-206807). https://ntrs.nasa.gov/citations/19980018321
- [4] David Darling. (2003). The complete Book of Spaceflight from Apollo 1 to Zero Gravity. John Wiley & Sons, Inc.
- [5] Dong, X., Hu, C., Long, T., & Li, Y. (2016). Numerical Analysis of Orbital Perturbation Effects on Inclined Geosynchronous SAR. *Sensors*, *16*(9), Article 9. https://doi.org/10.3390/s16091420
- [6] Ellis, J. R. (2010). Modeling, Dynamics, and Control of Tethered Satellite Systems. *Springer*, 73–96.
- [7] Ellis, J. R., & Hall, C. D. (2010). Out-of-plane librations of spinning tethered satellite systems. *Celestial Mechanics and Dynamical Astronomy*, 106(1), 39-67. https://doi.org/10.1007/s10569-009-9239-9

2025,10(55s) e-ISSN: 2468-4376

https://www.jisem-journal.com/ Research Article

- [8] El-samahy, A. A., & Shamseldin, M. A. (2018). Brushless DC motor tracking control using self-tuning fuzzy PID control and model reference adaptive control. *Ain Shams Engineering Journal*, 9(3), 341–352. https://doi.org/10.1016/j.asej.2016.02.004
- [9] Gerasimov D., Ortega R., & Nikiforov V. (2018a). Adaptive Control of Multivariable Systems with Reduced Knowledge of High Frequency Gain: Application of Dynamic Regressor Extension and Mixing Estimators, *IFAC-Papers OnLine*, 51(15), 886–890. https://doi.org/10.1016/j.ifacol.2018.09.108
- [10] Gerasimov D. N., Ortega R., & Nikiforov V. O. (2018b). Relaxing the high-frequency gain sign assumption in direct model reference adaptive control, *European Journal of Control*, 43, 12–19. https://doi.org/10.1016/j.ejcon.2018.06.002
- [11] Gonçalves, L. D., Rocco, E. M., & de Moraes, R. V. (2015). Analysis of the influence of orbital disturbances applied to an artificial lunar satellite. *Journal of Physics: Conference Series*, 641(1), 012028. https://doi.org/10.1088/1742-6596/641/1/012028
- [12] Hashemi, K. E., Akella, M. R., & Pak, C. (2015). Tracking error convergence for multi-input multi-output model reference adaptive control with known nonminimum phase zeros. *2015 54th IEEE Conference on Decision and Control (CDC)*, 489–494. https://doi.org/10.1109/CDC.2015.7402247
- [13] Iñarrea, M., Lanchares, V., Pascual, A. I., & Salas, J. P. (2014). Attitude stabilization of electrodynamic tethers in elliptic orbits by time-delay feedback control. *Acta Astronautica*, *96*, 280–295. https://doi.org/10.1016/j.actaastro.2013.12.011
- [14] Jo J. H., Park I. K., Choe N., & Choi M. (2011). The Comparison of the Classical Keplerian Orbit Elements, Non-Singular Orbital Elements (Equinoctial Elements), and the Cartesian State Variables in Lagrange Planetary Equations with J2 Perturbation: Part I, *Journal of Astronomy and Space Science*, 28 (1), 37–54. https://doi.org/10.5140/JASS.2011.28.1.037
- [15] Larsen, M. B. (2010). *Modeling and Control of Electrodynamic Tethers an Energy and Topology Approach*. Technical University of Denmark.
- [16] Misra, A. K. (2008). Dynamics and control of tethered satellite systems. *Acta Astronautica*, 63(11–12), 1169–1177. https://doi.org/10.1016/j.actaastro.2008.06.020
- [17] Misra A.K, & Modi V. J. (1986). A survey on the dynamics and control of tethered satellite systems. *International Conference on Tethers in Space*, 54.
- [18] Modi, V. J., & Misra, A. K. (1979). On the deployment dynamics of tether connected two-body systems. *Acta Astronautica*, *6*(9), 1183–1197. https://doi.org/10.1016/0094-5765(79)90064-X
- [19] Ortega R., Gerasimov D. N., Barabanov N. E., & Nikiforov V. O. (2019). Adaptive Control of Linear Multivariable Systems Using Dynamic Regressor Extension and Mixing Estimators: Removing the High-Frequency Gain Assumptions, *Automatica*, 110, 108589. https://doi.org/10.1016/j.automatica.2019.108589
- [20] Polycarpou M. M. (1996). Stable Adaptive Neural Control Scheme for Nonlinear Systems, *IEEE Transactions on Automatic Control*, 41 (3), 447–451. https://doi.org/10.1109/9.486648
- [21] Pankaj, S., Kumar, J. S, & Nema, R. K. (2011). Comparative Analysis of MIT Rule and Lyapunov Rule in Model Reference Adaptive Control Scheme, *Innovative Systems Design and Engineering* 2(4), 154–162.
- [22] Rao, M. P. R. V., & Hassan, H. A. (2004). New adaptive laws for model reference adaptive control using a non-quadratic Lyapunov function. Automatika, 45(3-4), 155–159. https://doi.org/10.1109/melcon.2004.1346879
- [23] Scheeres, D. J. (1999). Satellite Dynamics about Small Bodies: Averaged Solar Radiation Pressure Effects. *The Journal of the Astronautical Sciences*, *47*(1-2), 25–46. https://doi.org/10.1007/BF03546208

2025,10(55s) e-ISSN: 2468-4376

https://www.jisem-journal.com/

#### **Research Article**

- [24] Scheeres, D. J., Marzari, F., Tomasella, L., & Vanzani, V. (1998). ROSETTA mission: Satellite orbits around a cometary nucleus. *Planetary and Space Science*, 46(6-7), 649–671. https://doi.org/10.1016/S0032-0633(97)00200-6
- [25] Scheeres, D. J., Ostro, S. J., Hudson, R. S., DeJong, E. M., & Suzuki, S. (1998). Dynamics of Orbits Close to Asteroid 4179 Toutatis. *Icarus*, 132(1), 53–79. https://doi.org/10.1006/icar.1997.5870
- [26] Slotine J.-J. E., & Li W. (1991). Applied Nonlinear Control, Pearson Education, New Jersey.
- [27] Tirop P. & Jingrui Z. (2017). Application of Hamilton Principle in the Control of Tethered Satellite System Pendular Motion, *Aerospace Europe CEAS 2017 Conference*, Bucharest, Romania, 99–110. https://doi.org/10.13111/2066-8201.2018.10.2.10
- [28] Wang D., & Huang J. (2005). Neural Network-Based Adaptive Dynamic Surface Control for a Class of Uncertain Nonlinear Systems in Strict-Feedback Form, *IEEE Transactions on Neural Networks*. 16 (1), 195–202. https://doi.org/10.1109/TNN.2004.839354
- [29] Williams, P. (2009). Dynamic multibody modeling for tethered space elevators. *Acta Astronautica*, 65(3–4), 399–422. https://doi.org/10.1016/j.actaastro.2008.11.016
- [30] Williams, P., Hyslop, A., Stelzer, M., & Kruijff, M. (2009). YES2 optimal trajectories in presence of eccentricity and aerodynamic drag. *Acta Astronautica*, *64*(7-8), 745–769. https://doi.org/10.1016/j.actaastro.2008.11.007
- [31] Zabolotnov, Y. M., & Naumov, O. N. (2012). Motion of a descent capsule relative to its center of mass when deploying the orbital tether system. *Cosmic Research*, 50(2), 177–187. https://doi.org/10.1134/S0010952512020098
- [32] Zhao G. W., Sun, L., & Huang. H. (2014). Thrust Control of Tethered Satellite with a Short Constant Tether in Orbital Maneuvering. *Proceedings of the Institution of Mechical Engineers, Part G*, Journal of Aerospace Engineering, 228 (14), 2569–2586. https://doi.org/10.1177/0954410014521151
- [33] Zhong R., & Zhu Z. H. (2014). Optimal Control of Nanosatellite Fast Deorbit using Electrodynamic Tether, Journal of Guidance, Control, and Dynamics, 37(4), 1182–1194. https://doi.org/10.2514/1.62154